research papers

Acta Crystallographica Section A

Refinement of crystal structural parameters and charge density using convergent-beam electron diffraction – the rhombohedral phase of LaCrO$_3$

Kenji Tsuda,[a]* Yoichiro Ogata,[a] Kazunari Takagi,[a] Takuya Hashimoto[b] and Michiyoshi Tanaka[a]

[a]Institute of Multidisciplinary Research for Advanced Materials, Tohoku University, Sendai 980-8577, Japan, and [b]Department of Applied Physics, College of Humanities and Sciences, Nihon University, 3-25-40 Sakurajousui, Setagaya-ku, Tokyo 156-8550, Japan. Correspondence e-mail: k_tsuda@tagen.tohoku.ac.jp

Atom positions and anisotropic Debye–Waller factors of the rhombohedral phase of LaCrO$_3$ have been refined simultaneously with the low-order structure factors, using a structure-analysis method of convergent-beam electron diffraction (CBED) proposed by Tsuda & Tanaka [*Acta Cryst.* (1999), A**55**, 939–954]. The method is based on the least-squares fitting between full dynamical calculations and energy-filtered intensities of two-dimensional higher-order Laue-zone (HOLZ) and zeroth-order Laue-zone (ZOLZ) CBED patterns. The positions of the oxygen atoms have been determined with a high precision. Clear anisotropy of the thermal vibrations of the oxygen atoms has been successfully determined by the CBED method for the first time. The charge transfer from the La and Cr atoms to the O atoms has been found from the deformation charge-density map.

1. Introduction

In recent years, quantitative analyses of convergent-beam electron diffraction (CBED) for determining crystal structural parameters (low-order structure factors, atom positions, Debye–Waller factors *etc.*) have been reported by many researchers (Vincent *et al.*, 1984*a,b*; Zuo *et al.*, 1989, 1993, 1997, 1999; Tanaka & Tsuda, 1990, 1991; Deininger *et al.*, 1994; Tsuda & Tanaka, 1995, 1999; Saunders *et al.*, 1995, 1996, 1999*a,b*; Holmestad *et al.*, 1995; Nüchter *et al.*, 1998*a,b*; Jansen *et al.*, 1998; Wu *et al.*, 1999; Streltsov *et al.*, 2001). The method has the following advantages in contrast to the X-ray and neutron diffraction methods:

(i) *Nanometre-size crystal structure analysis:* CBED patterns can be obtained from specimen areas of a few nm in diameter. Thus, the CBED method enables us to conduct the structure determination of not only perfect crystals but also local areas of crystals.

(ii) *Dynamical diffraction effect:* the CBED intensities contain phase information on crystal structure factors through the strong dynamical effect.

(iii) *Site-selective analysis:* incident electrons form Bloch states in a specimen also due to the strong dynamical diffraction effect, each Bloch state being concentrated on specific atom positions. The use of the Bloch states allows site-selective structure analysis, or structure determination weighted for specific atom sites.

(iv) *High sensitivity to charge distribution:* structure factors of low-order reflections for electron diffraction are more sensitive to the distributions of valence electrons than those for X-ray diffraction.

We proposed a fully dynamical method to refine atom positions and Debye–Waller factors using CBED patterns with higher-order Laue-zone (HOLZ) reflections for the first time (Tanaka & Tsuda, 1990, 1991; Tsuda & Tanaka, 1995). The use of HOLZ reflections is essential for the method because small displacements of atoms can be sensitively detected using HOLZ reflections with large reciprocal vectors. The method is based on the least-squares fitting between dynamical calculations and experimental intensities measured by imaging plates. The method was successfully applied to refine the structural parameters of the low-temperature phase of SrTiO$_3$. The experimental intensities in this case were acquired from a thin specimen area without the use of any energy filter. The fitting of the intensities was carried out using both integrated intensities (zero-dimensional data) and one-dimensional line profiles of HOLZ reflections.

The use of two-dimensional CBED intensities provides much more information on structural parameters. It enables us to perform accurate fitting between experimental and theoretical intensities, thus improving the accuracy and reliability of the analysis. We extended our method for refining crystal structural parameters using CBED so as to fit the theoretical calculations with the experimental intensities of energy-

Table 1
Atom positions of the rhombohedral phase of LaCrO$_3$.

Site	Wyckoff position	Coordinate
La	2(a)	1/4, 1/4, 1/4
Cr	2(b)	0, 0, 0
O	6(e)	x(O), $-x$(O) + 1/2, 1/4

filtered two-dimensional zeroth-order Laue-zone (ZOLZ) and HOLZ CBED patterns (Tsuda & Tanaka, 1999). For this purpose, we developed a new energy-filter transmission electron microscope JEM-2010FEF, which can take CBED patterns covering high angles of up to 10° with small distortion (Tsuno *et al.*, 1997; Tanaka *et al.*, 1998). We have also developed an analysis program (*MBFIT*) to refine structural parameters, which is based on many-beam Bloch-wave calculations and nonlinear least-squares fitting. Using this method, we refined the atom positions and isotropic and anisotropic Debye–Waller factors of CdS.

The present method can be applied to the determination of charge-density distribution because the low-order Fourier coefficients of the potential (low-order structure factors for

Table 2
Refined values of the positional parameter (fractional coordinate) and anisotropic Debye–Waller factors of the rhombohedral phase of LaCrO$_3$; the values obtained by a neutron powder diffraction experiment using Rietveld analysis (Oikawa *et al.*, 2000) are shown in the right column for comparison.

Position and Debye–Waller factor (Å^2)	CBED	Neutron diffraction
x(O)	−0.30621 (2)	−0.30589 (32)
U_{11}(La)	0.008274 (4)	0.0085 (6)
U_{12}(La)	−0.002674 (2)	−0.0027 (4)
U_{11}(Cr)	0.005678 (3)	0.0041 (10)
U_{12}(Cr)	−0.001871 (2)	−0.0010 (7)
U_{11}(O)	0.01130 (4)	0.0104 (6)
U_{33}(O)	0.01456 (3)	0.0141 (11)
U_{12}(O)	−0.00787 (4)	−0.0066 (8)
U_{23}(O)	−0.001521 (5)	−0.0016 (4)

electron diffraction), which are sensitive to valence electrons, can be refined together with the atom positions and Debye–Waller factors. Through Poisson's equation, the structure factors for electron diffraction are converted to those of X-ray diffraction, or the Fourier coefficients of the charge density. According to the nature of Poisson's equation, a small change in the low-order structure factors for X-rays causes a large change in those of electron diffraction. Furthermore, the accuracy of the measurements of low-order structure factors using X-ray diffraction is strongly affected by the extinction effect. Therefore, the determination of the low-order structure factors for electron diffraction by the electron diffraction method has an advantage in determining more accurately low-order structure factors for X-ray diffraction, compared with
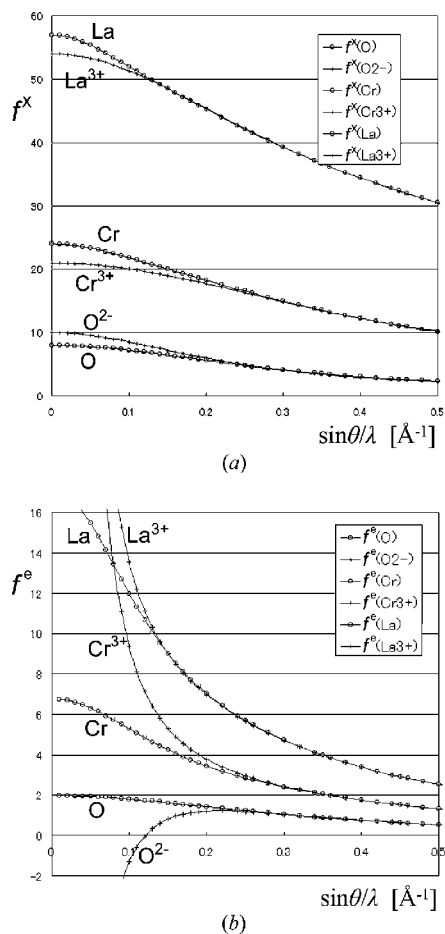

Figure 1
Atomic scattering factors (*a*) for X-rays and (*b*) for electrons. The differences in the scattering factors between the neutral and ionized atoms at low scattering angles are noted.
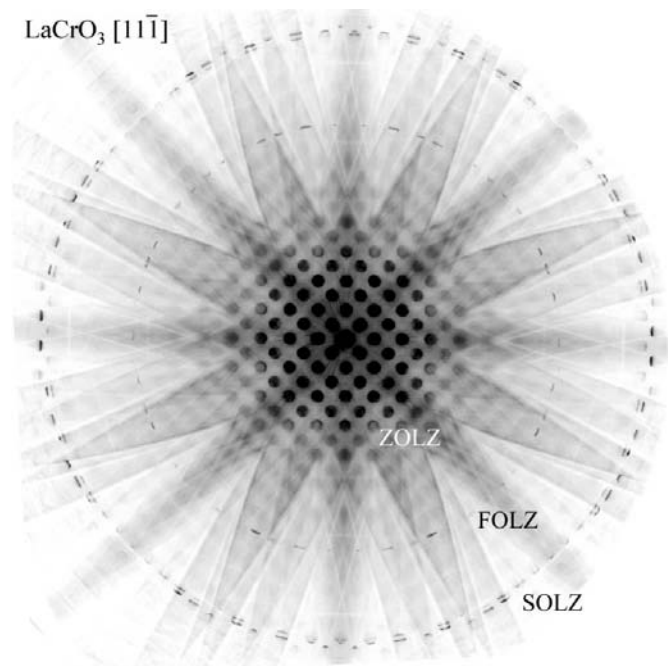

Figure 2
A CBED pattern of the rhombohedral phase of LaCrO$_3$ taken with [11$\bar{1}$] incidence at 573 K

the X-ray diffraction method. Refinements of the low-order structure factors using ZOLZ CBED patterns were performed by Saunders *et al.* (1995, 1996), Nüchter *et al.* (1998*a*) and Zuo *et al.* (1999). It should be noted that the accurate determina-

tion of Debye–Waller factors, which can be performed successfully by our refinement method with the use of HOLZ reflections, is crucial to obtaining high-precision low-order structure factors for X-rays. Thus, the present method would
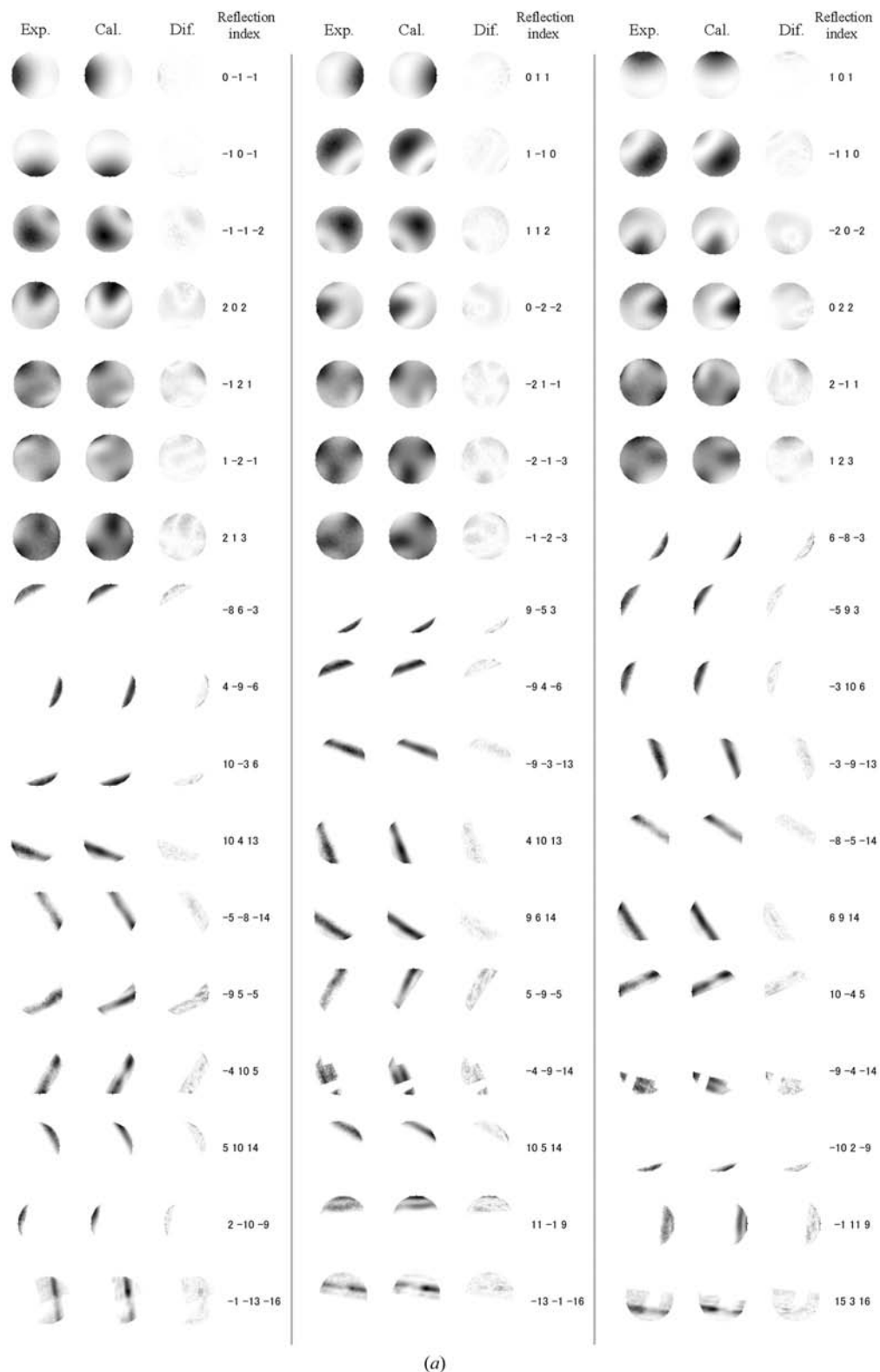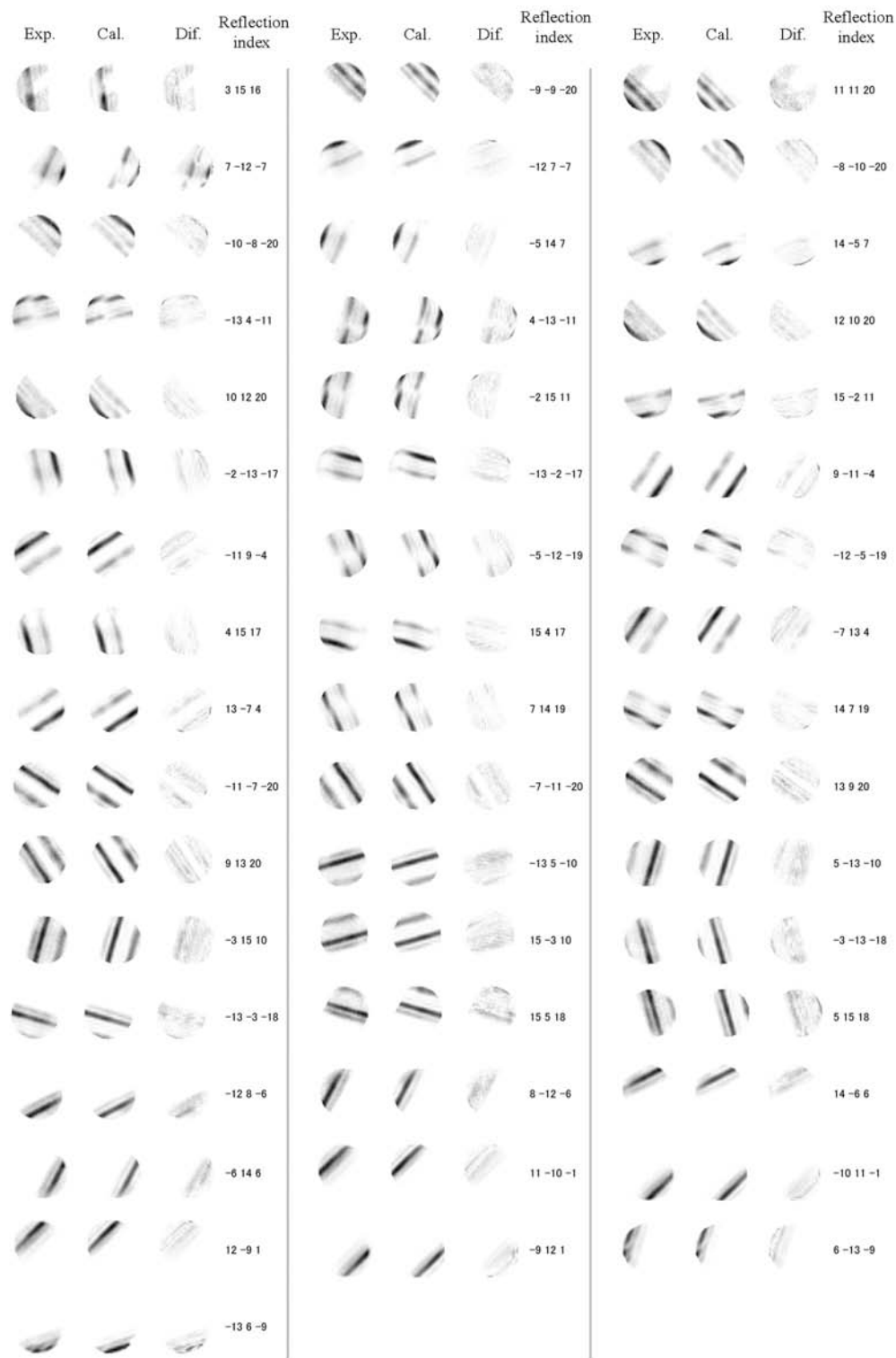

Figure 3
Final results of the fitting. The patterns in the left, center and right columns respectively show experimental, calculated and difference patterns.

have a potential to determine the behavior of valence electrons more accurately than the X-ray diffraction method and the electron diffraction method, which uses only ZOLZ reflections.

In the present paper, atom positions and anisotropic Debye–Waller factors of the rhombohedral phase of $LaCrO_3$ are refined simultaneously with the low-order structure factors using the present method for the first time. The electrostatic

(b)

Figure 3 (continued)

potential and charge-density distributions are obtained from the refined structural parameters.

2. Experimental method and analysis procedure

$LaCrO_3$ is a material for the interconnector of solid oxide fuel cells. It is known that $LaCrO_3$ has two structural phase transformations at approximately 2000 and 537 K. The phase above 2000 K is expected to have the cubic perovskite structure (Geller & Raccah, 1970). The two phases below 2000 K have distorted perovskite structures. It was reported that the space group of the phases above and below the transition temperature of 537 K are rhombohedral $R\bar{3}m$ (Höfer & Kock, 1993) and orthorhombic $Pbnm$ (Khattak & Cox, 1977; Berjoan et al., 1980), respectively. Prior to the structure refinement, we determined using the CBED method that the space groups above and below the transition temperature are respectively $R\bar{3}c$ and $Pbnm$ (Hashimoto et al., 2000). The relation between the rhombohedral axes and the pseudo-cubic axes is given by $\mathbf{a}_r = \mathbf{a}_c + \mathbf{c}_c$, $\mathbf{b}_r = \mathbf{a}_c + \mathbf{b}_c$ and $\mathbf{c}_r = \mathbf{b}_c + \mathbf{c}_c$, where $\mathbf{a}_r$, $\mathbf{b}_r$ and $\mathbf{c}_r$ are lattice parameters of the rhombohedral lattice and $\mathbf{a}_c$, $\mathbf{b}_c$ and $\mathbf{c}_c$ are those of the pseudo-cubic lattice. In the present paper, the incident-beam directions and reflection indices are expressed by the rhombohedral system. The atom positions of the rhombohedral phase of $LaCrO_3$ are given in Table 1.

The $LaCrO_3$ polycrystalline powder was supplied from Nikkato Co. Ltd. The powder was pressed into a pellet and sintered at 1470 K for 4 h in air, followed by cooling to room temperature at a rate of 200 K h^{-1}. The specimens for CBED experiments were prepared by crushing the pellets and dispersing the fragments on microgrids. The CBED experiments were conducted using the Ω-filter transmission electron microscope JEM-2010FEF (Tanaka et al., 1998). Intensities of CBED patterns were recorded on imaging plates (IP). The accelerating voltage of the electron microscope was determined to be 100.7 kV from a HOLZ line pattern of silicon using the method described by Tsuda & Tanaka (1995).

According to the procedure described by Tsuda & Tanaka (1999), the distortions of the CBED patterns were corrected by assuming analytical expressions of the distortions owing to the aberration of the lenses and the energy filter (radial, spiral and elliptical distortions). The weak remaining background intensities due to thermal diffuse scattering (TDS) were subtracted by reference to background intensities just outside the CBED discs.

The structural parameters are refined by a nonlinear least-squares fitting so as to minimize the residual sum of squares S, or the sum of the squared differences between the experimental CBED intensities and the theoretical CBED intensities. S is defined as $S = \sum_i w_i [I_i^{exp} - s I_i^{cal}(\mathbf{r}, B, F_g)]^2$, where I_i^{exp} is the ith experimental intensity, $I_i^{cal}(\mathbf{r}, B, F_g)$ is the calculated intensity for atom positions $\mathbf{r}$, Debye–Waller factors B and low-order structure factors F_g, w_i is a weight factor and s is a scale factor common to all the calculated intensities. We have set the weight factor $w_i = w_{LZ}/(\sigma_i^{exp})^2$, where σ_i^{exp} is the experimental error of I_i^{exp}. w_{LZ} is an additional weight factor to decrease the weight of ZOLZ reflections in S. Since intensities

of ZOLZ reflections are more than roughly 10^2 times those of HOLZ reflections and rather insensitive to positional parameters and Debye–Waller factors, the weights of ZOLZ reflections should be decreased using w_{LZ} for precise determination of the positional parameters and Debye–Waller factors. The nonlinear least-squares fitting is carried out by the analysis program MBFIT that we have developed (Tsuda & Tanaka, 1999).

In the present analysis, the low-order crystal structure factors for electron diffraction, which are sensitive to valence electrons, are refined together with the atom positions and Debye–Waller factors. The electrostatic potential and charge-density distribution are obtained using the refined low-order structure factors.

The structure factors for electron diffraction F_g^e is proportional to the Fourier coefficients of the electrostatic potential V_g as $V_g = F_g^e h^2/(8\pi\varepsilon_0 m_e e^2 \Omega)$, where h, ε_0, m_e, e and Ω are Planck's constant, the dielectric constant of vacuum, the rest mass of an electron, the charge of an electron and the volume of the unit cell, respectively. Thus, the electrostatic potential $V(\mathbf{r})$ is obtained by

$$V(\mathbf{r}) = \sum_g F_g^e \exp(2\pi i \mathbf{g} \cdot \mathbf{r}) h^2/(8\pi\varepsilon_0 m_e e^2 \Omega). \quad (1)$$

The structure factors for electron diffraction F_g^e can be transformed into the structure factors for X-ray diffraction F_g^X, or the Fourier coefficients of the charge density $\rho(\mathbf{r})$, using the following relation derived from Poisson's equation (e.g. Spence & Zuo, 1992):

$$F_g^X = \sum_i Z_i \exp(-B_i s^2) \exp(-2\pi i \mathbf{g} \cdot \mathbf{r}_i) - 8\pi\varepsilon_0 h^2 s^2 F_g^e/m_e e^2, \quad (2)$$

where Z_i is the atomic number of the ith atom and $s = \sin\theta/\lambda = |g|/2$. Thus, the charge density $\rho(\mathbf{r})$ is obtained by

$$\rho(\mathbf{r}) = \sum_g F_g^X \exp(2\pi i \mathbf{g} \cdot \mathbf{r})/\Omega. \quad (3)$$

According to the nature of Poisson's equation, a small change in the low-order structure factors for X-rays causes a large change in those for electrons. That is, the determination of the low-order F_g^e by the CBED method has an advantage in determining more accurately the low-order F_g^X, compared with the X-ray diffraction method. It should be noted that Debye–Waller factors are contained in the transformation from F_g^e to F_g^X. Thus, the accurate determination of Debye–Waller factors, which can be performed successfully by our refinement method with the use of ZOLZ and HOLZ reflections, is crucial to obtaining high-precision low-order structure factors for X-rays from the structure factors for electrons.

These features are evidently seen in atomic scattering factors. Fig. 1(a) shows the atomic scattering factors of X-rays f^X for neutral and ionized atoms of La, Cr and O as a function of $\sin\theta/\lambda$. The difference between f^X for a neutral atom and that for an ionized atom is confined in the region in which $\sin\theta/\lambda$ is smaller than roughly 0.25 $Å^{-1}$. The difference is largest at $\sin\theta/\lambda = 0$, where the value of f^X is equal to the

total number of electrons Z of the atom. The difference at $\sin\theta/\lambda = 0$ is 25% even for a light element like oxygen and is only about 5% for lanthanum. Atomic scattering factors for X-rays f^X and electrons f^e are related by the Mott formula

$$f^e = (Z - f^X)m_e e^2/8\pi\varepsilon_0 h^2 s^2, \qquad (4)$$

which is derived from Poisson's equation (*e.g.* Spence & Zuo, 1992). Fig. 1(*b*) shows the atomic scattering factors of electrons f^e for the neutral and ionized atoms. It is seen that the difference between the neutral and ionized atoms is remark-
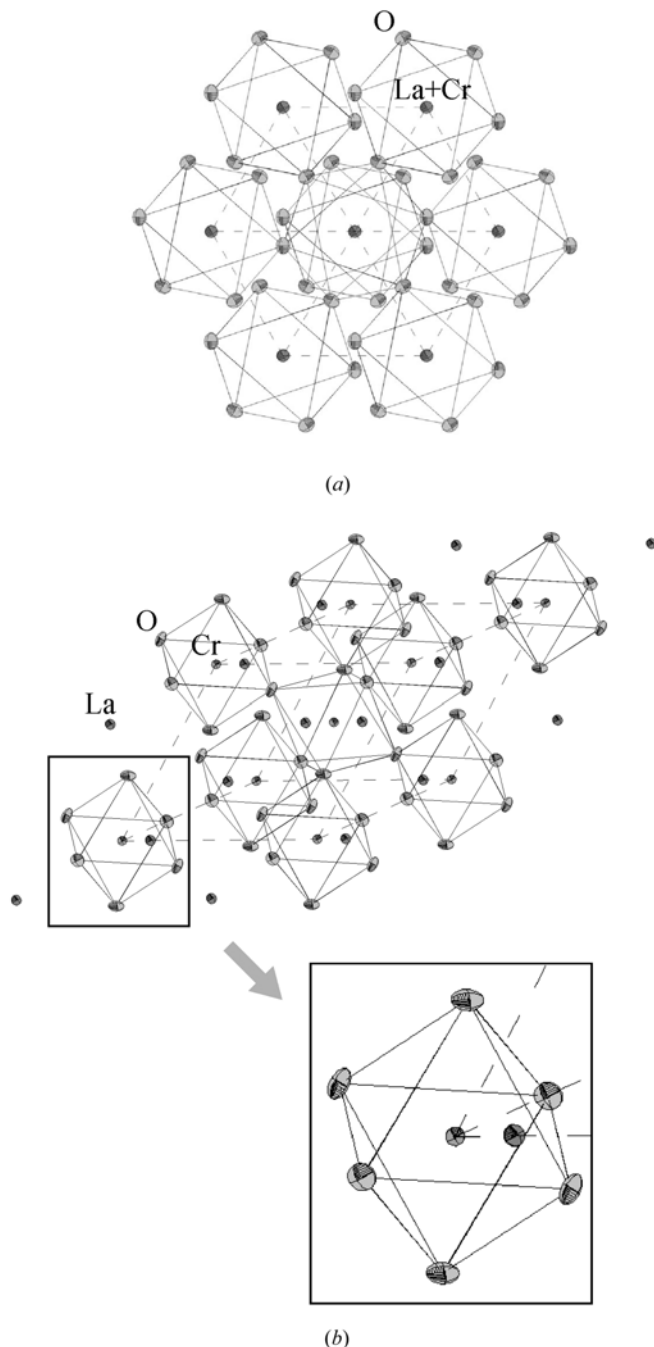

Figure 4
ORTEP diagrams of the fitting result viewed from (*a*) the [111] direction and (*b*) the [1̄12] direction. An octahedron of (*b*) is enlarged in the inset.
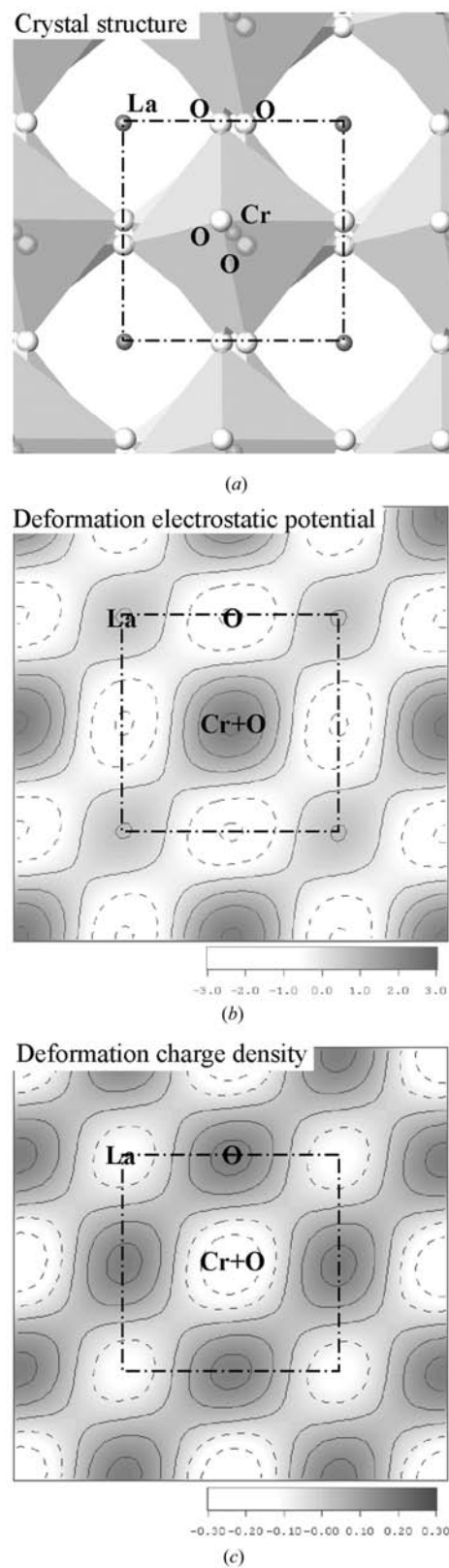

Figure 5
Crystal structure of the rhombohedral phase of (*a*) LaCrO₃, (*b*) deformation electrostatic potential and (*c*) deformation charge density projected in the [11̄1] direction. The solid lines and dotted lines of the contour maps indicate positive and negative values. The intervals of the contour lines of the maps (*b*) and (*c*) are 0.75 V and 0.075 e Å⁻², respectively.

ably enhanced in the region of low scattering angles. It is very clear from Fig. 1 that the difference in valence-electron distributions is observed more sensitively in the crystal structure factors for electron diffraction than in those for X-ray diffraction.

3. Results

3.1. Refinements

Fig. 2 shows an energy-filtered CBED pattern of the rhombohedral phase of $LaCrO_3$ taken with the $[11\bar{1}]$ incidence at a specimen temperature of 573 K using a heating specimen holder. The $[11\bar{1}]$ corresponds to the [100] direction in the notation of the cubic phase. The pattern was obtained from a few nm-diameter area in a single domain with an acceptance energy of 0 ± 10 eV. ZOLZ reflections are seen at the center of the pattern. HOLZ (FOLZ and SOLZ) reflections appear as two rings in the outer part, the SOLZ reflections having large reciprocal vectors with $\sin\theta/\lambda \sim 1.9$ Å^{-1}. It should be noted that the FOLZ reflections are sensitive to the positions and Debye–Waller factors of the O atoms because the FOLZ reflections are generated by the rotation of the oxygen octahedra.

After the distortion correction and background subtraction, two-dimensional intensities of 20 ZOLZ reflections and 80 HOLZ (FOLZ and SOLZ) reflections were extracted from the CBED pattern of Fig. 2. The total number of data points was 118 466, which consists of 39 220 points of ZOLZ reflections and 79 246 points of HOLZ reflections.

From the results of the convergence tests, 757 reflections were used in the dynamical calculations. 256 weak reflections among the 757 reflections were treated by the generalized Bethe potential (GBP) method (Ichikawa & Hayakawa, 1977).

The parameters to be refined in the fitting are the coordinate $x(O)$ of the O site, anisotropic Debye–Waller factors of all atoms, $U_{11}(La)$, $U_{12}(La)$, $U_{11}(Cr)$, $U_{12}(Cr)$, $U_{11}(O)$, $U_{33}(O)$, $U_{12}(O)$ and $U_{23}(O)$, low-order structure factors of three ZOLZ reflections F_{101}, $F_{1\bar{1}0}$ and F_{112}, scale factor s, specimen thickness t and 200 geometrical parameters to adjust finely the positions of reflection discs. The three reflections 101, $1\bar{1}0$ and 112 have values of $\sin\theta/\lambda$ smaller than 0.25 Å^{-1}.

The nonlinear least-squares fitting was performed in the following steps. In the first step, the positional parameter $x(O)$ and anisotropic Debye–Waller factors were refined, where the additional weight factor w_{LZ} to reduce the weight of the ZOLZ reflections was set to 0.002. In this step, the values of the low-order structure factors were assumed to be the values calculated from the atomic scattering factors of the neutral atoms. In the second step, the low-order structure factors were refined using the values of the positional parameter and Debye–Waller factors obtained in the first step. The w_{LZ} was set to 0.02 for increasing the weights of ZOLZ reflections, which are sensitive to the low-order structure factors. In the final step, all of the parameters were refined simultaneously.

The final results of the fitting are shown in Fig. 3. The patterns in the left, center and right columns respectively show experimental, calculated and difference patterns. The calculated patterns are seen to agree very well with the experimental patterns. The refined values of the positional parameter (fractional coordinate) and anisotropic Debye–Waller factors are given in Table 2. The standard deviations of the refined parameters in parentheses were simply evaluated according to the error-propagation rule as described by Tsuda & Tanaka (1995). The values of the standard deviations are considered to be appreciably underestimated because of the large number of data points of the two-dimensional pattern. The values obtained by a neutron powder diffraction experiment using the Rietveld analysis (Oikawa et al., 2000), which was conducted based on the space group determined by us, are
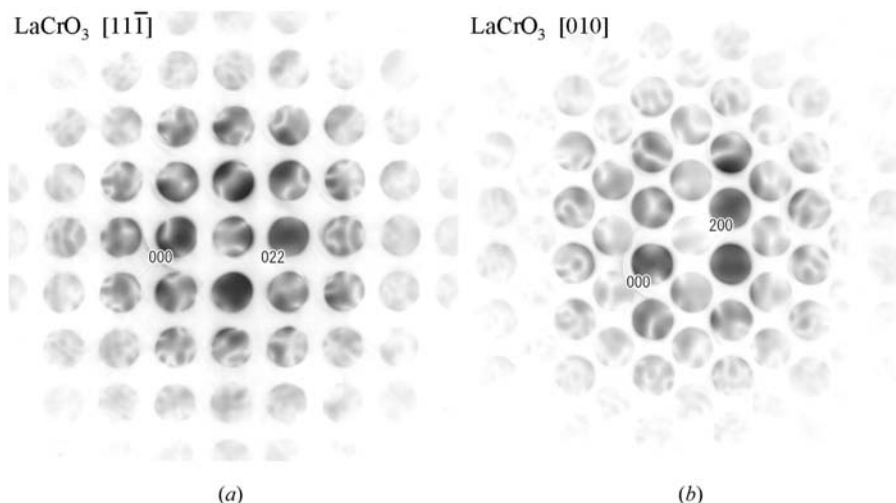

Figure 6
CBED patterns of the rhombohedral phase of $LaCrO_3$ taken at 573 K with the 022 Bragg excitation near the $[11\bar{1}]$ incidence and with the 200 Bragg excitation near the [010] incidence, respectively.

Table 3
Refined values of the low-order structure factors of reflections 101, 1$\bar{1}$0 and 112; the values calculated from the atomic scattering factors of neutral atoms and ionized atoms are shown for comparison.

g	$\sin\theta/\lambda$ (Å^{-1})	F_g refined	F_g neutral	F_g ionized (Å)
101	0.128	−7.542 (3)	−8.012	−7.238
1$\bar{1}$0	0.181	20.233 (3)	19.120	20.761
112	0.183	20.451 (2)	19.596	21.009

Table 4
Refined values of the low-order structure factors of reflections 201, 200 and 022; the values calculated from the atomic scattering factors of neutral atoms and ionized atoms are shown for comparison.

g	$\sin\theta/\lambda$ (Å^{-1})	F_g refined	F_g neutral	F_g ionized (Å)
201	0.213	−3.3169 (2)	−3.499	−3.175
200	0.222	−11.5847 (3)	−12.639	−11.591
022	0.257	21.5340 (3)	21.698	21.642

shown in the right column for comparison. It is seen that the values agree well with the CBED values.

The refined values of the low-order structure factors are given in Table 3. The values calculated from the atomic scattering factors of neutral atoms and ionized atoms are shown for comparison. The refined values are seen to be intermediate between those of neutral atoms and ionized atoms.

3.2. Atom positions and anisotropic Debye–Waller factors

The crystal structure of LaCrO$_3$ determined by the present fitting is shown in the style of the *ORTEP* diagram, in which anisotropic Debye–Waller factors are displayed as thermal ellipsoids. Fig. 4(a) shows the diagram of the fitting result viewed from the [111] direction. It is seen that the neighboring octahedra in the [111] direction rotate in directions opposite to each other with respect to the [111] axis. As a result, the O atoms deviate from the positions of the cubic perovskite structure, in which the two atoms are superposed in this projection. Fig. 4(b) shows the diagram of the fitting result viewed from the [$\bar{1}\bar{1}$2] direction. An octahedron in Fig. 4(b) is enlarged in the inset. It is seen that the thermal ellipsoid is elongated in the directions perpendicular to the bond connecting an O atom at a vertex and the Cr atom at the center of the octahedron. Such clear anisotropy of the thermal vibration of the oxygen atom has been found by the CBED method for the first time.

3.3. Electrostatic potential and charge density projected along [11$\bar{1}$]

Electrostatic potential and charge density of LaCrO$_3$ projected in the [11$\bar{1}$] direction were calculated with the refined parameters of atom positions, Debye–Waller factors and the low-order structure factors of reflections 101, 1$\bar{1}$0 and 112. Fig. 5(a) shows the crystal structure of the rhombohedral phase of LaCrO$_3$ projected in the [11$\bar{1}$] direction. Fig. 5(b)

shows the projected deformation electrostatic potential, or the difference between the electrostatic potential calculated with the fitting result and that calculated with the neutral atoms. It is seen that the potential is increased at the La and Cr+O sites and decreased at the O sites. Fig. 5(c) shows the projected deformation charge density or the difference between the charge density calculated with the fitting result and that calculated with neutral atoms. The charge transfer from the La and Cr atoms to the O atoms is clearly seen. Details of the deformation charge density will be discussed in §4.3.

3.4. Three-dimensional charge density

To obtain three-dimensional distribution of the charge density, we successively refined the low-order structure factors of reflections 201, 200 and 022 using energy-filtered CBED patterns taken with different incidences. Figs. 6(a) and 6(b) show the CBED patterns taken at $T = 573$ K with the 002 Bragg excitation near the [11$\bar{1}$] incidence and the 200 Bragg excitation near the [010] incidence, respectively, to enhance the intensities of these low-order reflections. Similarly, after the distortion correction and background subtraction, two-dimensional intensity data of 86 ZOLZ reflections were extracted from these CBED patterns. The total number of data points was 119415. The refined values of the low-order structure factors are shown in Table 4. The values calculated from the atomic scattering factors of the neutral atoms and ionized atoms are shown for comparison.

From these low-order structure factors together with the already refined 101, 1$\bar{1}$0 and 112 reflections, the three-dimensional distribution of the charge density of the rhombohedral phase of LaCrO$_3$ was constructed. The three-dimensional deformation charge density is visualized in Fig. 7. The charge transfer from the Cr atom to the O atoms is clearly seen.

The structure factor of the 222 reflection, which could not be determined using these CBED patterns, was set to be the value calculated with the ionized atoms. As is the
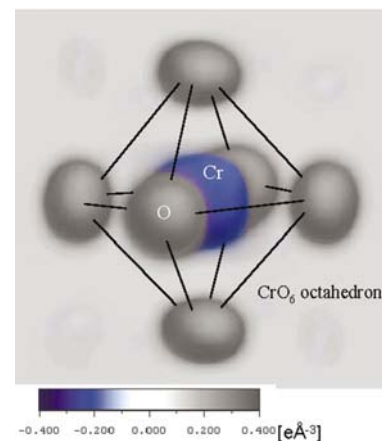
Figure 7
Three-dimensional visualization of the deformation charge density obtained from the present analysis. The color scale bar is attached to the map. The color of the low-density region was set to be translucent.

case for the other refined low-order structure factors, the value of the structure factor of the 222 reflection is expected to be in between the value calculated with the ionized atoms and that calculated with the neutral atoms. When the value of the structure factor of the 222 reflection is changed from the value for the ionized atoms to that for the neutral atoms, only slight elongations of the charges at the Cr+O and O sites in the [111] direction was seen in the deformation charge-density map.

4. Discussion

4.1. Bloch states

The positions and anisotropic Debye–Waller factors of the oxygen atoms have been successfully determined in the present analysis though the atomic number of oxygen ($Z = 8$) is considerably smaller than those of La ($Z = 57$) and Cr ($Z = 24$) atoms. This can be explained from the viewpoint of the Bloch states formed by incident electrons.
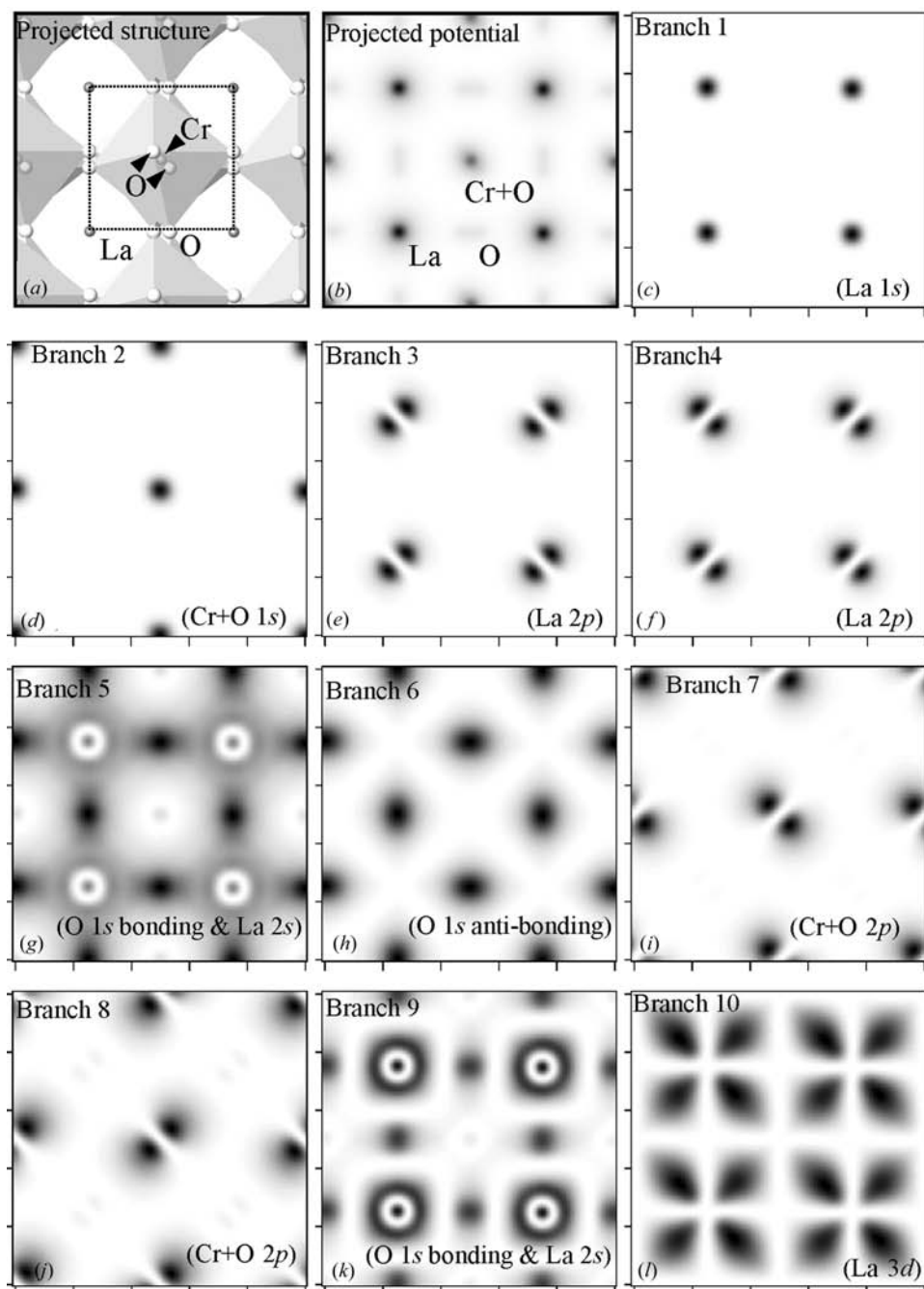

Figure 8
(a) Projected structure and (b) projected electrostatic potential of LaCrO$_3$ in the [11$\bar{1}$] direction. Electron-density distributions of branches 1 to 10 are shown in (c) to (l), respectively.

Figs. 8(a) and 8(b) show the projected structure and projected electrostatic potential of LaCrO$_3$ in the [11$\bar{1}$] direction, respectively. It is seen that the projected structure is composed of rows of La atoms (La site), rows of Cr and O atoms (Cr+O site) and rows of O atoms (O site). Figs. 8(c) to 8(l) show the electron-density distributions of branches 1 to 10 of the Bloch states, respectively. These were calculated at an accelerating voltage of 100.7 kV using 109 ZOLZ reflections. Each Bloch state is seen to have density maxima at specific positions. For example, the electron densities of branches 1 and 2 are concentrated on the rows of La atoms (Fig. 8c) and on the rows of Cr and O atoms (Fig. 8d), respectively. The electron density of branch 5 is concentrated strongly on the rows of O atoms and weakly on the rows of La atoms. These Bloch states can be assigned to atomic states or hybridized states, which are also indicated in Fig. 8.

Figs. 9(a) and 9(b) show a section of the dispersion surface and the excitation of the Bloch states of LaCrO$_3$ along the direction of $\mathbf{g}_{112}$ around the [11$\bar{1}$] incidence. It is seen that branch 5, which has density maxima at the O sites, has the greatest excitation at the zone-axis incidence. Thus, the
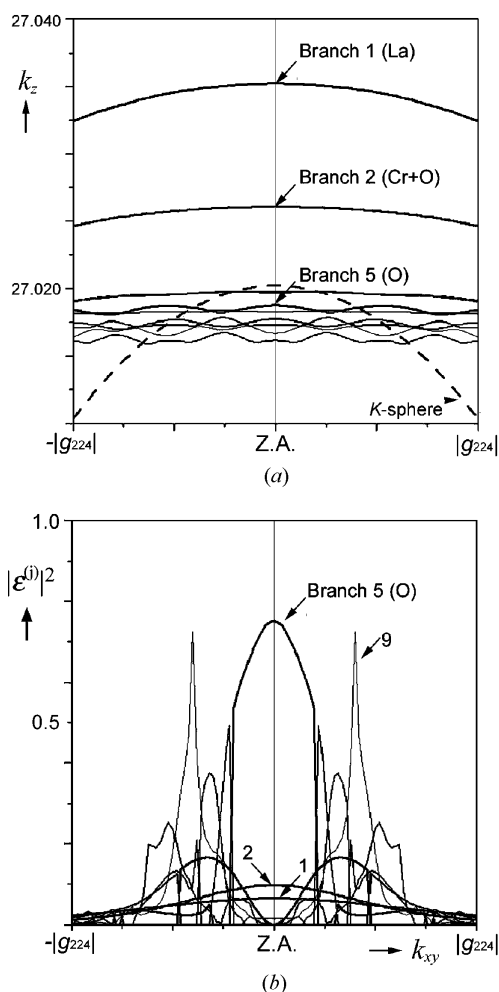
sensitivity for the O atoms is strongly enhanced at the [11$\bar{1}$] zone-axis incidence, at which the CBED pattern of Fig. 2 was obtained. This accounts for the successful determination of the positions and the anisotropic thermal vibrations of the O atoms.

This site-selective characteristic of the Bloch states can be extensively used for improving the accuracy of the parameters refined by the present method. CBED patterns taken with changing the tilt of the incident beam have excitations of different Bloch states concentrating on specific sites, thus being sentitive to different atomic sites. Therefore, the combined use of the other CBED patterns taken with different tilt of the incident beam is expected to provide much further information to refine structural parameters and to enable us to determine more of the low-order structure factors.

4.2. Comparison with the neutron diffraction experiment

To compare the atom positions and anisotropic Debye–Waller factors of the present result with those of the neutron diffraction experiments (Oikawa *et al.*, 2000), we simulated the CBED patterns using the atom positions and Debye–Waller factors determined by the neutron diffraction. Figs. 10(a) and 10(b) show the CBED patterns of several SOLZ reflections simulated by the present result and by the neutron diffraction data, respectively. In the same manner as Fig. 3, the patterns in the left, center and right columns respectively show experimental, calculated and difference patterns. The present result (Fig. 10a) shows small differences between the experimental and the calculated patterns. In contrast, considerable differences are seen between the experimental CBED patterns and the patterns simulated by the neutron diffraction data (Fig. 10b). It should be noted that in Fig. 10(b) one of the two peaks in each calculated CBED disc is larger than the corresponding peak in the experimental CBED disc. It was found that the peak is caused by the Bloch state concentrating on the Cr+O site (branch 2 of Fig. 8d), the other peak being caused by the O site (branch 5 of Fig. 8g). Thus, the disagreement of the peak intensities can be attributed to the difference between the Debye–Waller factors of the Cr atoms for the present analysis and those for the neutron diffraction. In fact, this is seen in Table 2 where the Debye–Waller factors of the Cr atoms, U_{11}(Cr) and U_{12}(Cr), determined by the present analysis are slightly larger than those found by neutron diffraction. This indicates that the present method can distinguish such small differences in the structural parameters.

4.3. Deformation charge density

The charge transfer from the La and Cr atoms to the O atoms is clearly seen in the deformation charge-density maps of Fig. 5(c). From the fact that the nominal valence numbers of the La, Cr and O atoms are respectively 3+, 3+ and 2−, the amount of the transferred charge at the La site is expected to be larger than that at the Cr+O site. However, the minimum of the deformation charge density at the La site is seen to be higher than the minimum at the Cr+O site. This fact indicates

Figure 9
(a) A section of the dispersion surface and (b) the excitation of the Bloch states of LaCrO$_3$ along the direction of $\mathbf{g}_{112}$ around the [11$\bar{1}$] incidence.

that the transferred charge is appreciably delocalized for the heavier La atoms but localized for the Cr and O atoms at the Cr+O and O sites.

The deficit charge at the Cr site is seen to be almost spherical. Since the Cr^{3+} ion in $LaCrO_3$ has three $3d$ electrons that occupy three t_{2g} states, it is expected that the Cr ion will form a nearly spherical electron distribution. Thus, the present results are consistent with this conjecture.

On the other hand, the excess charge at the O site is seen to be elongated in the same directions as the thermal ellipsoids of the O atoms. The bonding charge between the Cr and O atoms was hardly seen in the deformation charge-density maps. In order to discuss bonding charge in more detail, more low-order structure factors should be determined using the site-selective feature of the Bloch states as mentioned in §4.1

4.4. Error introduced by the conversion from f^e to f^X

The error introduced by the transformation from the structure factors for electron diffraction to those for X-ray diffraction is discussed here using atomic scattering factors.

From the Mott formula, the following relation is derived for $|\delta f^X / f^X|$ (Watanabe *et al.*, 1969):

$$|\delta f^X / f^X| = |\delta f^e / f^e|(Z - f^X)/f^X, \qquad (5)$$

where f^X, f^e, δf^X, δf^e and Z are atomic scattering factors for X-rays and electrons, their estimated errors and the atomic number, respectively. This relation indicates that, in the course of the transformation from f^e to f^X, the relative error of f^X is given by the relative error of f^e multiplied by the factor $(Z - f^X)/f^X$. Fig. 11 shows the factor $(Z - f^X)/f^X$ for La, Cr and O atoms as a function of $\sin\theta/\lambda$. It is seen that $(Z - f^X)/f^X$ is less than 1 in the region of low scattering angles, at which the atomic scattering factor is sensitive to valence electrons. Therefore, the CBED method can determine the low-order F_g^X more accurately than the X-ray diffraction method.

5. Concluding remarks

We have applied the CBED structure analysis method proposed by Tsuda & Tanaka (1999) to the rhombohedral phase of $LaCrO_3$. The atom positions and Debye–Waller factors have been refined simultaneously with low-order structure factors for the first time. The positions and aniso-tropic Debye–Waller factors of the O atoms have been successfully determined with high precision owing to the site-selective characteristics of dynamical diffraction. Clear anisotropy of the thermal vibrations of the O atoms has been detected by CBED for the first time. The deformation elec-trostatic potential and deformation charge density have been constructed from the refined structural parameters, revealing clear charge transfer from the La and Cr atoms to the O atoms. It should be noted that the precise atom positions and Debye–Waller factors are indispensable for obtaining the charge density from the low-order structure factors for electron diffraction. Thus, the present method is the unique technique that can determine the crystal structure and charge density from a nanometre-size area of specimens.

The present method can be extensively applied to the charge-density determination of the perovskite and related materials revealing charge ordering and orbital ordering phenomena, which are closely related to the colossal magneto-resistance and the high-T_c superconductivity. Though the materials are frequently composed of very small domains owing to twin structures and/or characteristic phase separa-tions, the CBED technique allows us to obtain diffraction intensity data from a single domain. We have already begun the charge-density determination of the orbital-ordering phase of $LaMnO_3$, for which the ordering of e_g orbitals of the Mn $3d$ electrons was observed using the resonant X-ray scattering (RXS) technique (Murakami *et al.*, 1998). We have
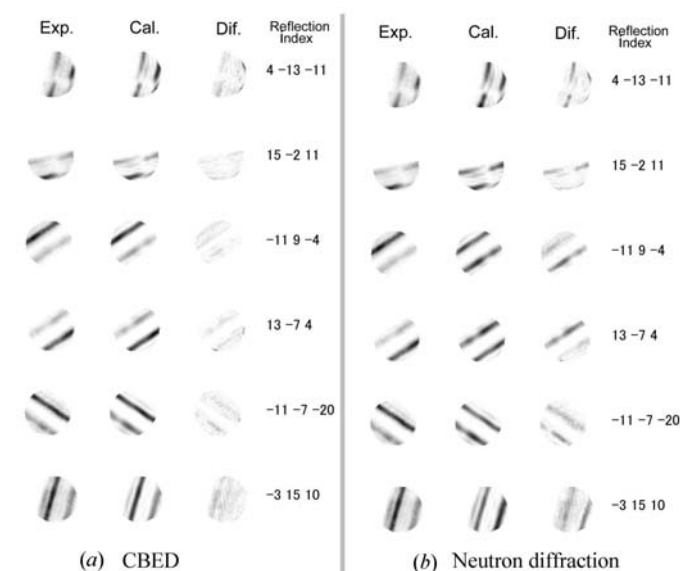

Figure 10
CBED patterns of some SOLZ reflections simulated (*a*) by the present data and (*b*) by neutron diffraction data.

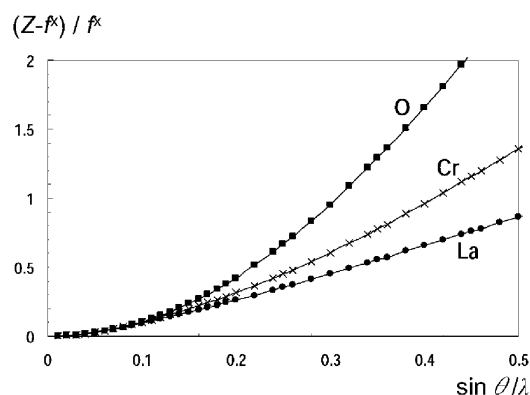**Figure 11**
Plot of $(Z - f^X)/f^X$ as a function of $\sin\theta/\lambda$ (Å^{-1}).

already obtained a preliminary result of the charge density of $LaMnO_3$, in which the electron distribution is not spherical but extends toward the O sites. The details will be described in a forthcoming paper.

The present method to date needs enormous time to simultaneously refine many structural parameters. This will be reduced by the use of parallel computations. Parallel computation will also be useful for extending the application of the present method to the analysis of local structures of imperfect crystals, which requires the use of a lower-symmetry space group and a superlattice cell.

References

Berjoan, R., Romand, C. & Coutures, J. P. (1980). *High Temp. Sci.* **13**, 173–188.

Deininger, C., Necker, G. & Mayer, J. (1994). *Ultramicroscopy*, **54**, 15–30.

Geller, S. & Raccah, P. M. (1970). *Phys. Rev. B*, **2**, 1167–1172.

Hashimoto, T., Takagi, K., Tsuda, K., Tanaka, M., Yoshida, K., Tagawa, H. & Dokiya, M. (2000). *J. Electrochem. Soc.* **147**, 4408–4410.

Höfer, H. E. & Kock, W. F. (1993) *J. Electrochem. Soc.* **140**, 2889–2894.

Holmestad, R., Zuo, J. M., Spence, J. C. H., Høier, R. & Horita, Z. (1995). *Philos. Mag.* A**72**, 579–601.

Ichikawa, M. & Hayakawa, K. (1977). *J. Phys. Soc. Jpn*, **42**, 1957–1964.

Jansen, J., Tang, D., Zandbergen, H. W. & Schenk, H. (1998). *Acta Cryst.* A**54**, 91–101.

Khattak, C. P. & Cox, D. E. (1977). *Mater. Res. Bull.* **12**, 463–472.

Murakami, Y., Hill, J. P., Gibbs, D., Blume, M., Koyama, I., Tanaka, M., Kawata, H., Arima, T., Tokura, Y., Hirota, K. & Endoh, Y. (1998). *Phys. Rev. Lett.* **81**, 582–585.

Nüchter, W., Weichkenmeier, A. L. & Mayer, J. (1998*a*). *Phys. Status Solidi*, **166**, 367–379.

Nüchter, W., Weichkenmeier, A. L. & Mayer, J. (1998*b*). *Acta Cryst.* A**54**, 147–157.

Oikawa, K., Kamiyama, T., Hashimoto, T., Shimojyo, Y. & Morii, Y. (2000). *J. Solid State Chem.* **154**, 524–529.

Saunders, M., Bird, D. M., Holbrook, O. F., Midgley, P. A. & Vincent, R. (1996). *Ultramicroscopy*, **65**, 45–52.

Saunders, M., Bird, D. M., Zaluzec, N. J., Burgess, W. G., Preston, A. R. & Humphreys, C. J. (1995). *Ultramicroscopy*, **60**, 311–323.

Saunders, M., Fox, A. G. & Midgley, P. A. (1999*a*). *Acta Cryst.* A**55**, 471–479.

Saunders, M., Fox, A. G. & Midgley, P. A. (1999*b*). *Acta Cryst.* A**55**, 480–488.

Spence, J. C. H. & Zuo, J. M. (1992). *Electron Microdiffraction.* New York: Plenum Press.

Streltsov, V. A., Nakashima, P. N. H. & Johnson, A. W. S. (2001). *J. Phys. Chem. Solids*, **62**, 2109–2117.

Tanaka, M. & Tsuda, K. (1990). *Proc. XIIth ICEM*, edited by L. D. Peachy & D. B. Williams, Vol. 2, pp. 518–519. San Francisco Press.

Tanaka, M. & Tsuda, K. (1991). *Proc. Microbeam Analysis*, edited by D. G. Howitt, pp. 145–146. San Francisco Press.

Tanaka, M., Tsuda, K., Terauchi, M., Tsuno, K., Kaneyama, T., Honda, T. & Ishida, M. (1998). *J. Microsc.* **194**, 219–227.

Tsuda, K. & Tanaka, M. (1995). *Acta Cryst.* A**51**, 7–19.

Tsuda, K. & Tanaka, M. (1999). *Acta Cryst.* A**55**, 939–954.

Tsuno, K., Kaneyama, T., Honda, T., Tsuda, K., Terauchi, M. & Tanaka, M. (1997). *J. Electron Microsc.* **46**, 357–368.

Vincent, R., Bird, D. M. & Steeds, J. W. (1984*a*). *Philos. Mag.* A**50**, 745–763.

Vincent, R., Bird, D. M. & Steeds, J. W. (1984*b*). *Philos. Mag.* A**50**, 765–786.

Watanabe, D., Uyeda, R. & Fukuhara, A. (1969). *Acta Cryst.* A**25**, 138–140.

Wu, M.-Y., Li, S.-Y., Zhu, J., Du, Z.-H. & Li, S.-L. (1999). *Acta Cryst.* A**56**, 189–192.

Zuo, J. M., Kim, M., O'Keeffe, M. & Spence, J. C. H. (1999). *Nature (London)*, **401**, 49–52.

Zuo, J. M., O'Keeffe, M., Rez, P. & Spence, J. C. H. (1997). *Phys. Rev. Lett.* **78**, 4777–4780.

Zuo, J. M., Spence, J. C. H., Downs, J. & Mayer, J. (1993). *Acta Cryst.* A**49**, 422–429.

Zuo, J. M., Spence, J. C. H. & Høier, R. (1989). *Phys. Rev. Lett.* **62**, 547–550.